

## AlSb nucleation induced anisotropic electron mobility in AlSb/InAs heterostructures on GaAs

L. Desplanque,<sup>1</sup> S. El Kazzi,<sup>1</sup> J.-L. Codron,<sup>1</sup> Y. Wang,<sup>2</sup> P. Ruterana,<sup>2</sup> G. Moschetti,<sup>3</sup> J. Grahn,<sup>3</sup> and X. Wallart<sup>1</sup>

<sup>1</sup>Institut d'Electronique, de Microelectronique et de Nanotechnologie, UMR-CNRS 8520, BP 60069, 59652 Villeneuve d'Ascq Cedex, France

<sup>2</sup>CIMAP UMR 6252 CNRS-ENSICAEN-CEA-UCBN, 6, Boulevard du Maréchal Juin, 14050 Caen Cedex, France

<sup>3</sup>Department of Microtechnology and Nanoscience (MC2), Microwave Electronics Laboratory, Chalmers University of Technology, SE-412 96 Göteborg, Sweden

(Received 27 April 2012; accepted 8 June 2012; published online 25 June 2012)

The influence of the growth conditions at the AlSb/GaAs interface on the electron mobility in AlSb/InAs heterostructures is investigated. We show that an excessive antimony flux during the initial stage of the AlSb buffer growth leads to a strong anisotropy of electron mobility in InAs between [110] and [1-10] crystallographic orientations. This anisotropy is attributed to the formation of trenches oriented along the [1-10] direction in the InAs channel. Transmission electron microscopy reveals that these trenches are directly related to twinning defects originating from the AlSb/GaAs interface. © 2012 American Institute of Physics. [<http://dx.doi.org/10.1063/1.4730958>]

The excellent intrinsic electron transport properties of InAs-based heterostructures are very appealing for both microwave/millimeter-wave low noise amplifier (LNA)<sup>1-3</sup> and for next generation of low power consumption MOSFET devices based on III-V materials.<sup>4-6</sup> However, since the pioneering works of Professor H. Kroemer's group in the early 1990s,<sup>7</sup> the introduction of such materials into industrial technologies is still challenging. The lack of maturity of InAs based heterostructures is primarily due to the lack of large size lattice matched semiconductor substrates which requires the use of a metamorphic approach to accommodate the mismatch with InP,<sup>8</sup> GaAs,<sup>9</sup> GaP,<sup>10</sup> or Si substrates.<sup>11</sup> The threading defects originating from the mismatch accommodation can cause severe degradation of future device performances and reliability. In a recent paper, we have reported on the anisotropic electron mobility in AlSb/InAs heterostructures grown on InP substrates and shown that this anisotropy is attributed to the presence of trenches in the InAs channel related to threading defects in the buffer layer.<sup>12</sup>

In this paper, we demonstrate that the density of trenches is directly related to the antimony overpressure during the AlSb nucleation layer on GaAs.

The samples were grown by molecular beam epitaxy (MBE) in a Riber Compact 21 equipped with solid source valve cells for group-V element evaporation. Group-III and -V element fluxes were calibrated using standard reflection high energy electron diffraction (RHEED) specular intensity oscillation technique. A typical Al evaporation rate of 0.8 ML s<sup>-1</sup> is used for the AlSb deposition. All the epilayers were grown from an exactly oriented semi-insulating GaAs (001) substrate.

After a 300 nm GaAs buffer layer grown at 580 °C, the temperature is decreased to 510 °C and stabilized for a few minutes with no As flux. The surface exhibits a (2 × 4) As-terminated surface reconstruction. To avoid As-Sb intermixing, the surface is exposed to an Sb flux for two minutes

once the reactor base pressure reaches the 10<sup>-9</sup> Torr range. A (2 × 8) surface reconstruction characteristic of an Sb-terminated GaAs surface is observed.<sup>13</sup> During the initial stage of the AlSb deposition, the formation of islands can be deduced from the spotty RHEED pattern. After a few minutes, a 2D-like (1 × 3) RHEED pattern is recovered revealing the coalescence of AlSb islands. In the first set of experiment, different Sb fluxes from 2.5 to 1 ML s<sup>-1</sup> are used all along the antimonide parts of the structure depicted in Figure 1 (samples A to D). After 50 nm of the AlSb nucleation layer grown at 510 °C, the growth temperature is increased to 540 °C for the remaining AlSb buffer and decreased again to 510 °C for the final AlGaSb part.

To observe the influence of the Sb overpressure during the buffer layer on the morphology of the InAs channel, two

Contact layer	InAs:Te (7×10 <sup>18</sup> cm <sup>-3</sup> )	5 nm
Protection layer	Al <sub>0.5</sub> In <sub>0.5</sub> As	4 nm
Schottky layer	AlSb	10 nm
Doping plane	Te = 4.5×10 <sup>12</sup> cm <sup>-2</sup>	
Spacer	AlSb	6.5 nm
Channel	InAs	15 nm
Bottom barrier	AlSb	10 nm
Buffer	Al <sub>0.8</sub> Ga <sub>0.2</sub> Sb	250 nm
Buffer	AlSb	550 nm
Nucleation layer	AlSb	50 nm
Buffer	GaAs	300 nm
Substrate	GaAs SI	

FIG. 1. Schematic of the Te doped AlSb/InAs heterostructure grown on GaAs (sample A, B, C, D and A'). For samples E and F, the growth is interrupted after the InAs channel.

TABLE I. Transport properties of AlSb/InAs heterostructures for different Sb overpressures (difference between Sb and Al fluxes) during antimonide layers. For sample A', the Sb fluxes were reduced only during the AlSb nucleation layer.

Sample reference	A	B	C	A'	D
Sb overpressure during AlSb nucleation layer ( $\text{ML s}^{-1}$ )	1.7	0.7	0.5	0.3	0.2
$N_s$ ( $\times 10^{12} \text{ cm}^{-2}$ )	-3.4	-3.0	-3.0	-3.4	-2.6
300 K VdP Electron mobility ( $300 \text{ K}$ ) ( $\text{cm}^2 \text{ V}^{-1} \text{ s}^{-1}$ )	15 100	18 600	20 400	19 400	22 000
300 K [110] Electron mobility ( $\text{cm}^2 \text{ V}^{-1} \text{ s}^{-1}$ )	10 800	14 600	16 900	16 500	19 700
300 K [1-10] Electron mobility ( $\text{cm}^2 \text{ V}^{-1} \text{ s}^{-1}$ )	22 000	21 900	23 200	20 700	23 200
77 K VdP Electron mobility ( $\text{cm}^2 \text{ V}^{-1} \text{ s}^{-1}$ )	25 000	36 600	44 900	39 200	54 600
77 K [110] Electron mobility ( $\text{cm}^2 \text{ V}^{-1} \text{ s}^{-1}$ )	16 100	24 400	30 900	27 700	39 500
77 K [1-10] Electron mobility ( $\text{cm}^2 \text{ V}^{-1} \text{ s}^{-1}$ )	60 500	57 100	67 100	49 100	67 200

specific samples with an Sb overpressure (difference between Sb and Al fluxes) of  $1.7 \text{ ML s}^{-1}$  and  $0.2 \text{ ML s}^{-1}$  are grown (sample E and F). These samples are similar to sample A and D, respectively, but we stop the growth just after the InAs channel to avoid any roughening of the surface by the top InAlAs barrier.

Finally, in order to distinguish between the role of the Sb flux during the AlSb nucleation layer and its impact on the remaining part of the buffer and heterostructure part, we perform another growth with an Sb overpressure of  $0.3 \text{ ML s}^{-1}$  during the first 50 nm of AlSb (sample A'). The remaining part of the epilayer is grown with an Sb flux of  $2.5 \text{ ML s}^{-1}$  as for sample A.

Atomic force microscopy (AFM) using a digital NanoScope III system working in the tapping mode is used for the surface morphology analysis of the samples. Their structural properties are investigated by high resolution transmission electron microscopy (HRTEM) using a JEOL 2010 FEG instrument operating at 200 kV. Eventually, transport properties of the heterostructures are measured at room temperature and 77 K using Hall bridge oriented in both [110] and [1-10] crystallographic orientations to determine the electron mobility in the two directions as well as a Van der Pauw configuration for measuring the mean mobility value.

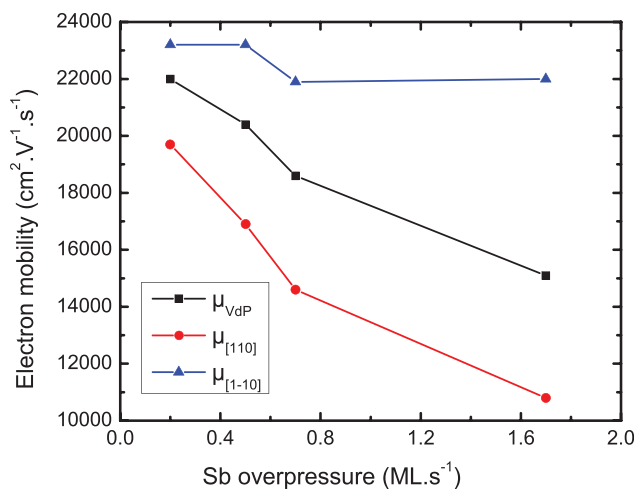


FIG. 2. Hall electron mobility measured on AlSb/InAs heterostructures using a Van der Pauw configuration ( $\mu_{\text{VdP}}$ , squares), Hall Bridges oriented along [1-10] direction ( $\mu_{[1-10]}$ , triangles) and Hall Bridges oriented along [110] direction ( $\mu_{[110]}$ , circles) in function of Sb overpressure during antimonide layer MBE growth.

The transport properties of the heterostructures obtained with different Sb overpressures are summarized in Table I. As can be noticed in Figure 2, the room temperature electron mobility in the [110] crystallographic orientation is strongly reduced by increasing the Sb flux during the growth whereas that in the [1-10] direction is nearly constant. The evolution of the Van der Pauw mobility is consistent with this observation with a mean value between the two orthogonal orientations.

Concerning the sheet carrier density, a higher Sb flux during the doping plane leads to a slightly higher doping efficiency. Since the [1-10] electron mobility is nearly not affected by this variation, it cannot explain the strong reduction of electron mobility in the [110] orientation.

The ratios of electron mobility ( $\mu$ ) measured in the [1-10] and [110] directions are plotted in Figure 3. An increasing Sb overpressure leads to a linear increase of this ratio both at room temperature and 77 K. The anisotropy of mobility measured on the sample with a reduced Sb overpressure during the AlSb nucleation layer (triangles in Figure 3) follows exactly the evolution observed with the first set of samples. This result demonstrates that the origin of electron mobility anisotropy is directly related to Sb overpressure during the first stage of the AlSb growth.

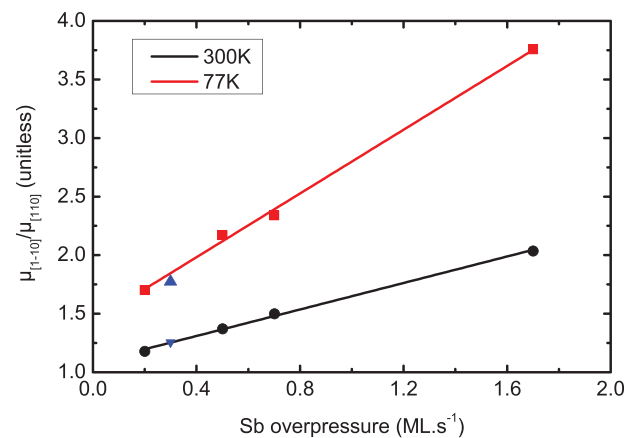


FIG. 3. Ratio of electron mobility measured on Hall Bridges oriented, respectively, in the [1-10] and [110] orientations at 300 K (circles) and 77 K (squares) for different Sb overpressures during the antimonide layers of the structure. Down- and up- triangles show, respectively, the value of electron mobility measured at 300 K and 77 K on the same heterostructure with an Sb overpressure of  $0.3 \text{ ML s}^{-1}$  during the initial 50 nm part of the AlSb buffer, the Sb overpressure was  $1.7 \text{ ML s}^{-1}$  during the rest of the buffer layer and AlSb/InAs heterostructure.

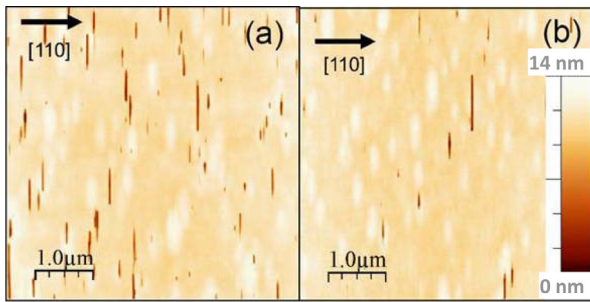


FIG. 4. AFM measurement on sample E (a) and F (b) with, respectively, 1.7 and 0.3 ML s<sup>-1</sup> Sb overpressure during antimonide layers.

The morphologies of samples E and F are shown on the AFM images of Figures 4(a) and 4(b). As can be deduced from these images, the anisotropy of mobility observed on the previous samples is directly related to the density of trenches oriented in the [1-10] direction, the interaction of these defects with traveling electrons in the [110] direction being much more detrimental. From the AFM image, the density of trenches for a 1.7 ML s<sup>-1</sup> Sb overpressure is about  $3 \times 10^8 \text{ cm}^{-2}$ , whereas it is about  $0.7 \times 10^8 \text{ cm}^{-2}$  for a 0.2 ML s<sup>-1</sup> Sb overpressure. In Figure 5, the cross section TEM observations along the [110] zone axis of the former sample show that the trenches are induced by threading defects coming from the AlSb buffer layer. Their orientation with respect to the growth direction (about 35°) indicates that these defects are in (111) planes. The HRTEM images of Figures 5(b) and 5(d) evidence that these defects are micro-twins.

A semi-quantitative understanding of the influence of the trench density (TD) on the mobility can be highlighted considering the electron mean free path in the InAs 2D electron gas. In the [1-10] direction which is nearly not affected by the trenches, the measured mobility of 22 000 cm<sup>2</sup>/V s associated with a sheet carrier density of  $3 \times 10^{12} \text{ cm}^{-2}$  leads to an electron mean free path around 0.6 μm at room temperature. This means that the critical TD above which trenches will reduce the electron mean free path and hence the mobil-

ity amounts to  $2.5 \times 10^8 \text{ cm}^{-2}$ . This is in semi-quantitative agreement with our measurements for which a strong mobility reduction in the [110] direction is observed for a TD of  $3 \times 10^8 \text{ cm}^{-2}$  whereas the effect is less for a TD of  $0.7 \times 10^8 \text{ cm}^{-2}$ . At 77 K, of course, the mean free path increases (around 1.7 μm) and the effect of the trenches on the [110] mobility is stronger, even for the lowest TD.

Concerning the origin of micro-twins, it has been shown that, in the GaSb/GaAs system, the GaSb 2D growth promotes the formation of Lomer dislocations and the confinement of the strain at the hetero-interface.<sup>14</sup> On the contrary, 60° dislocations are predominantly generated in the case of 3D growth. Moreover, as evidenced in a recent investigation,<sup>15,16</sup> the Sb overpressure plays a crucial role on relaxation and formation of GaSb islands. A high Sb overpressure promotes the formation of large {111} faceted and relaxed islands elongated in the [110] direction. In the present work in which growth starts with the deposition of AlSb islands on GaAs, rapid AlSb oxidization prevents one from studying the early stages of the growth but the spotty RHEED pattern observed during the nucleation reveals that AlSb islands are initially formed. We can then infer that under high Sb overpressure, micro-twins are generated during the coalescence of the {111} advancing facets of the relaxed AlSb islands.

In conclusion, we have shown that Sb overpressure during the initial stage of the AlSb buffer layer growth governs the electron mobility in AlSb/InAs heterostructures. A high Sb overpressure induces threading defects in the (111) crystallographic planes that cause the formation of trenches oriented along the [1-10] direction in the InAs tensile strained channel. These trenches result in a poor electron mobility in the [110] direction. In light of these results, the optimum growth conditions for AlSb nucleation to achieve the highest mobility in the InAs channel are obtained by minimizing the Sb overpressure. This optimization should also increase the stability of the AlSb/InAs heterostructure, suppressing the oxidization of AlSb that could be exposed to air within the trenches. As a consequence, these results could lead to a

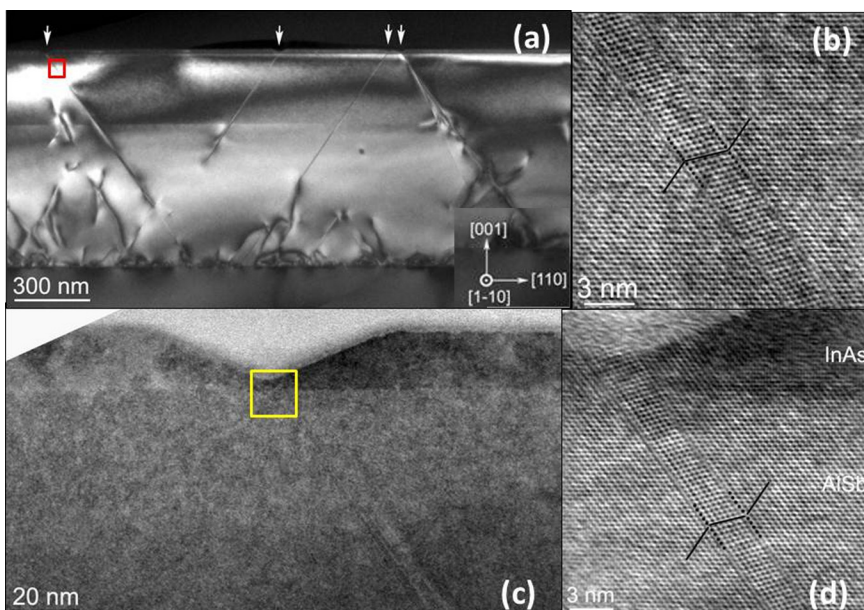


FIG. 5. Image (a) displays a TEM cross-section measurement ( $g=002$  dark field) on the sample with the highest Sb overpressure (sample E). The white arrows indicate the presence of trenches in the InAs layer coming from the threading defects originating from the AlSb/GaAs interface. Image (b) is an HRTEM image of a threading defect from the highlighted area of figure (a): The atomic configuration of the defect is underlined evidencing a micro-twin. Image (c) shows a TEM cross-section of one of the InAs trenches in sample E. Image (d) is a HRTEM image of the highlighted area of figure (c) showing the connection between the InAs trench and the micro-twin.

significant improvement of InAs-based transistor performances and reliability.

This work is supported by the national research agency under Projects MOS35 (Contract No. ANR-08-NANO-022), LowIQ (Contract No. ANR-08-NANO-022), and SMIC (Contract No. ANR-11-ASTR-031-03).

- <sup>1</sup>W. Kruppa, J. J. Boos, B. R. Bennett, N. A. Papanicolaou, D. Park, and R. Bass, *Electron. Lett.* **42**, 688 (2006).
- <sup>2</sup>M. Malmkvist, E. Lefebvre, M. Borg, L. Desplanque, X. Wallart, G. Dambrine, S. Bollaert, and L. Grahn, *IEEE Trans. Microwave Theory Tech.* **56**, 2685 (2008).
- <sup>3</sup>A. Noudeviwa, Y. Roelens, F. Danneville, A. Olivier, N. Wichmann, N. Waldhoff, S. Lepilliet, G. Dambrine, L. Desplanque, X. Wallart, G. Moschetti, J. Grahn, and S. Bollaert, *IEEE Trans. Electron Devices* **57**, 1903 (2010).
- <sup>4</sup>H. Ko, K. Takei, R. Kapadia, S. Chuang, H. Fang, P. W. Leu, K. Ganapathi, E. Plis, H. S. Kim, S.-Y. Chen, M. Madsen, A. C. Ford, Y.-L. Chueh, S. Krishna, S. Salahuddin, and A. Javey, *Nature (London)* **468**, 286 (2010).
- <sup>5</sup>H. Zhao, Y.-T. Chen, J. H. Yum, Y. Wang, F. Xue, and J. C. Lee, *Appl. Phys. Lett.* **96**, 102101 (2010).
- <sup>6</sup>S. H. Kim, M. Yokoyama, N. Taoka, R. Nakane, T. Yasuda, O. Ichikawa, N. Fukuhara, M. Hata, M. Takenaka, and S. Takagi, *Tech. Dig. - Int. Electron Devices Meet.* **2011**, 13.4.1.
- <sup>7</sup>H. Kroemer, *Physica E* **20**, 196 (2004).
- <sup>8</sup>L. Desplanque, D. Vignaud, and X. Wallart, *J. Cryst. Growth* **301**, 194 (2007).
- <sup>9</sup>H.-R. Blank, M. Thomas, K. C. Wong, and H. Kroemer, *Appl. Phys. Lett.* **69**, 2080 (1996).
- <sup>10</sup>S. El Kazzi, L. Desplanque, C. Coinon, Y. Wang, P. Ruterana, and X. Wallart, *Appl. Phys. Lett.* **97**, 192111 (2010).
- <sup>11</sup>K.-M. Ko, J.-H. Seo, D.-E. Kim, S.-T. Lee, Y.-K. Noh, M.-D. Kim, and J.-E. Oh, *Nanotechnology* **20**, 225201 (2009).
- <sup>12</sup>G. Moschetti, H. Zhao, P.-A. Nilsson, S. Wang, A. Kalabukhov, G. Dambrine, S. Bollaert, L. Desplanque, X. Wallart, and J. Grahn, *Appl. Phys. Lett.* **97**, 243510 (2010).
- <sup>13</sup>P. Laukkanen, R. E. Perälä, R. L. Vaara, I. J. Värynen, M. Kuzmin, and J. Sadowski, *Phys. Rev. B* **69**, 205323 (2004).
- <sup>14</sup>Y. Wang, P. Ruterana, L. Desplanque, S. El Kazzi, and X. Wallart, *Europhys. Lett.* **97**, 68011 (2012).
- <sup>15</sup>L. Desplanque, S. El Kazzi, C. Coinon, Y. Wang, P. Ruterana, and X. Wallart, in 23rd International Conference On Indium Phosphide and Related Materials, IPRM 2011, Berlin, Germany, 22–26 May 2011.
- <sup>16</sup>S. El Kazzi, L. Desplanque, X. Wallart, Y. Wang, and P. Ruterana, *J. Appl. Phys.* **111**, 123506 (2012).